Supplementary Information

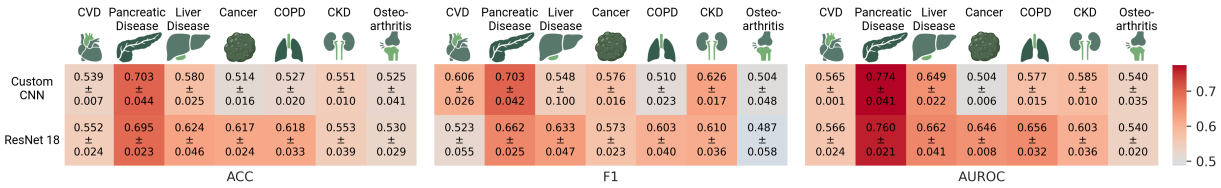

Supplementary Figure 1. Results of ResNet18 and a custom CNN model with fewer trainable parameters using whole-body MRI for 3-year preclinical risk assessment for cardiovascular disease (CVD), pancreatic disease, liver disease, cancer, chronic obstructive pulmonary disease (COPD), chronic kidney disease (CKD), osteoarthritis. The custom CNN consists of three 3D convolutional layers with kernel size 3, stride 1, and padding 1, each followed by batch normalization and $2 \times 2 \times 2$ max pooling. It ends with adaptive global average pooling and a fully connected layer for classification.

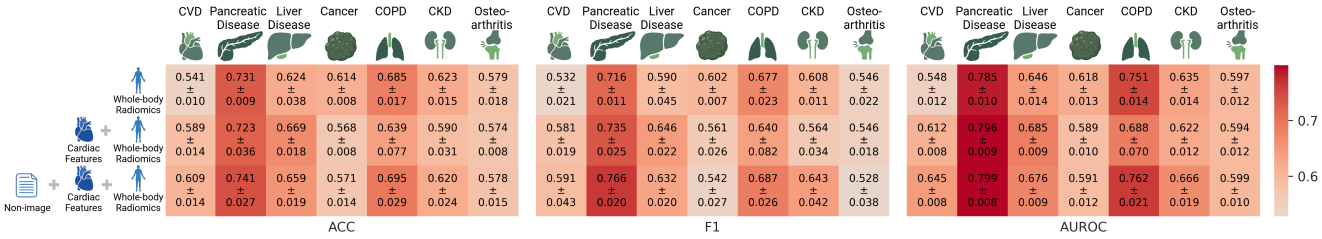

Supplementary Figure 2. Results of whole-body radiomics with cardiac features and non-image data fusion for 3-year preclinical risk assessment for cardiovascular disease (CVD), pancreatic disease, liver disease, cancer, chronic obstructive pulmonary disease (COPD), chronic kidney disease (CKD), osteoarthritis. The integration of cardiac features with whole-body radiomics results shows improved predictive accuracy for risk assessment of CVD and liver disease. A minor improvement in F1 and AUROC is observed by pancreatic disease. The observed findings demonstrate the known interplay between the cardiovascular, metabolic, and hepatic systems[1].

Model	Modality		Metric		
	Whole-body Radiomics	Non-image	ACC	F1	AUROC
RF		✓	**0.578 ± 0.009**	0.556 ± 0.010	0.612 ± 0.003
XGB		✓	0.565 ± 0.014	0.548 ± 0.014	0.585 ± 0.010
MLP		✓	0.558 ± 0.028	0.541 ± 0.064	0.592 ± 0.020
RF	✓		**0.541 ± 0.010**	0.532 ± 0.021	0.548 ± 0.012
XGB	✓		0.520 ± 0.016	0.520 ± 0.014	0.524 ± 0.017
MLP	✓		0.529 ± 0.020	0.535 ± 0.031	0.536 ± 0.020
RF	✓	✓	**0.545 ± 0.020**	0.537 ± 0.026	0.562 ± 0.009
XGB	✓	✓	0.531 ± 0.012	0.527 ± 0.020	0.544 ± 0.015
MLP	✓	✓	0.532 ± 0.021	0.557 ± 0.066	0.563 ± 0.027

Supplementary Table 1. Results of tabular models Random Forest (RF), eXtreme Gradient Boosting (XGB), and Mulit-Layer Perceptron (MLP) for cardiovascular disease (CVD) evaluated on the test dataset. Models are trained using different tabular data modalities: whole-body radiomics, non-image data, and a combination of whole-body radiomics and non-image data. The best-performing model based on accuracy is highlighted in bold and reported in Figure 2.

Model	Modality		Metric		
	Whole-body Radiomics	Non-image	ACC	F1	AUROC
RF		✓	**0.627 ± 0.013**	0.627 ± 0.020	0.698 ± 0.010
XGB		✓	0.597 ± 0.015	0.613 ± 0.017	0.646 ± 0.005
MLP		✓	0.608 ± 0.041	0.568 ± 0.064	0.671 ± 0.041
RF	✓		0.692 ± 0.026	0.695 ± 0.029	0.757 ± 0.016
XGB	✓		**0.731 ± 0.009**	0.716 ± 0.011	0.785 ± 0.010
MLP	✓		0.697 ± 0.035	0.697 ± 0.051	0.763 ± 0.030
RF	✓	✓	0.715 ± 0.036	0.724 ± 0.036	0.772 ± 0.014
XGB	✓	✓	**0.754 ± 0.020**	0.755 ± 0.022	0.798 ± 0.020
MLP	✓	✓	0.692 ± 0.010	0.709 ± 0.025	0.771 ± 0.003

Supplementary Table 2. Results of tabular models Random Forest (RF), eXtreme Gradient Boosting (XGB), and Mulit-Layer Perceptron (MLP) for pancreatic disease evaluated on the test dataset. Models are trained using different tabular data modalities: whole-body radiomics, non-image data, and a combination of whole-body radiomics and non-image data. The best-performing model based on accuracy is highlighted in bold and reported in Figure 2.

Model	Modality		Metric		
	Whole-body Radiomics	Non-image	ACC	F1	AUROC
RF		✓	**0.629 ± 0.022**	0.627 ± 0.017	0.689 ± 0.020
XGB		✓	0.512 ± 0.015	0.662 ± 0.016	0.640 ± 0.043
MLP		✓	0.537 ± 0.071	0.555 ± 0.114	0.542 ± 0.109
RF	✓		**0.624 ± 0.038**	0.590 ± 0.045	0.646 ± 0.014
XGB	✓		0.595 ± 0.035	0.544 ± 0.056	0.638 ± 0.020
MLP	✓		0.588 ± 0.030	0.537 ± 0.030	0.628 ± 0.038
RF	✓	✓	**0.637 ± 0.034**	0.606 ± 0.043	0.657 ± 0.019
XGB	✓	✓	0.600 ± 0.029	0.621 ± 0.015	0.623 ± 0.021
MLP	✓	✓	0.551 ± 0.035	0.564 ± 0.065	0.594 ± 0.042

Supplementary Table 3. Results of tabular models Random Forest (RF), eXtreme Gradient Boosting (XGB), and Mulit-Layer Perceptron (MLP) for Liver Disease evaluated on the test dataset. Models are trained using different tabular data modalities: whole-body radiomics, non-image data, and a combination of whole-body radiomics and non-image data. The best-performing model based on accuracy is highlighted in bold and reported in Figure 2.

Model	Modality		Metric		
	Whole-body Radiomics	Non-image	ACC	F1	AUROC
RF		✓	**0.489 ± 0.017**	0.479 ± 0.015	0.483 ± 0.014
XGB		✓	0.483 ± 0.014	0.477 ± 0.022	0.478 ± 0.019
MLP		✓	0.487 ± 0.025	0.507 ± 0.062	0.495 ± 0.014
RF	✓		0.590 ± 0.020	0.581 ± 0.028	0.609 ± 0.018
XGB	✓		**0.614 ± 0.008**	0.602 ± 0.007	0.618 ± 0.013
MLP	✓		0.530 ± 0.022	0.505 ± 0.042	0.529 ± 0.020
RF	✓	✓	0.581 ± 0.013	0.580 ± 0.015	0.605 ± 0.015
XGB	✓	✓	**0.623 ± 0.028**	0.604 ± 0.042	0.629 ± 0.015
MLP	✓	✓	0.513 ± 0.029	0.505 ± 0.039	0.507 ± 0.044

Supplementary Table 4. Results of tabular models Random Forest (RF), eXtreme Gradient Boosting (XGB), and Mulit-Layer Perceptron (MLP) for cancer evaluated on the test dataset. Models are trained using different tabular data modalities: whole-body radiomics, non-image data, and a combination of whole-body radiomics and non-image data. The best-performing model based on accuracy is highlighted in bold and reported in Figure 2.

Model	Modality		Metric		
	Whole-body Radiomics	Non-image	ACC	F1	AUROC
RF		✓	**0.698 ± 0.022**	0.725 ± 0.018	0.744 ± 0.022
XGB		✓	0.653 ± 0.035	0.686 ± 0.041	0.730 ± 0.010
MLP		✓	0.657 ± 0.038	0.660 ± 0.036	0.687 ± 0.038
RF	✓		**0.685 ± 0.017**	0.677 ± 0.023	0.751 ± 0.014
XGB	✓		0.654 ± 0.029	0.640 ± 0.046	0.734 ± 0.021
MLP	✓		0.651 ± 0.071	0.651 ± 0.058	0.703 ± 0.052
RF	✓	✓	**0.743 ± 0.017**	0.752 ± 0.018	0.774 ± 0.022
XGB	✓	✓	0.690 ± 0.012	0.708 ± 0.019	0.767 ± 0.017
MLP	✓	✓	0.631 ± 0.035	0.647 ± 0.031	0.699 ± 0.024

Supplementary Table 5. Results of tabular models Random Forest (RF), eXtreme Gradient Boosting (XGB), and Mulit-Layer Perceptron (MLP) for chronic obstructive pulmonary disease (COPD) evaluated on the test dataset. Models are trained using different tabular data modalities: whole-body radiomics, non-image data, and a combination of whole-body radiomics and non-image data. The best-performing model based on accuracy is highlighted in bold and reported in Figure 2.

Model	Modality		Metric		
	Whole-body Radiomics	Non-image	ACC	F1	AUROC
RF		✓	0.580 ± 0.032	0.579 ± 0.037	0.601 ± 0.024
XGB		✓	**0.595 ± 0.015**	0.595 ± 0.015	0.632 ± 0.004
MLP		✓	0.584 ± 0.021	0.622 ± 0.015	0.600 ± 0.022
RF	✓		0.585 ± 0.025	0.555 ± 0.029	0.643 ± 0.012
XGB	✓		**0.623 ± 0.015**	0.608 ± 0.011	0.635 ± 0.014
MLP	✓		0.597 ± 0.020	0.597 ± 0.020	0.645 ± 0.012
RF	✓	✓	0.598 ± 0.013	0.579 ± 0.020	0.649 ± 0.012
XGB	✓	✓	**0.636 ± 0.019**	0.612 ± 0.024	0.648 ± 0.025
MLP	✓	✓	0.636 ± 0.035	0.648 ± 0.049	0.674 ± 0.028

Supplementary Table 6. Results of tabular models Random Forest (RF), eXtreme Gradient Boosting (XGB), and Mulit-Layer Perceptron (MLP) for chronic kidney disease (CKD) evaluated on the test dataset. Models are trained using different tabular data modalities: whole-body radiomics, non-image data, and a combination of whole-body radiomics and non-image data. The best-performing model based on accuracy is highlighted in bold and reported in Figure 2.

Model	Modality		Metric		
	Whole-body Radiomics	Non-image	ACC	F1	AUROC
RF		✓	**0.560 ± 0.017**	0.538 ± 0.010	0.588 ± 0.012
XGB		✓	0.534 ± 0.007	0.483 ± 0.021	0.578 ± 0.012
MLP		✓	0.520 ± 0.017	0.493 ± 0.080	0.544 ± 0.026
RF	✓		**0.579 ± 0.018**	0.546 ± 0.022	0.597 ± 0.012
XGB	✓		0.574 ± 0.009	0.560 ± 0.013	0.588 ± 0.012
MLP	✓		0.550 ± 0.014	0.544 ± 0.037	0.561 ± 0.012
RF	✓	✓	**0.580 ± 0.019**	0.568 ± 0.020	0.606 ± 0.011
XGB	✓	✓	0.555 ± 0.023	0.541 ± 0.029	0.591 ± 0.021
MLP	✓	✓	0.541 ± 0.034	0.548 ± 0.058	0.559 ± 0.033

Supplementary Table 7. Results of tabular models Random Forest (RF), eXtreme Gradient Boosting (XGB), and Mulit-Layer Perceptron (MLP) for osteoarthritis evaluated on the test dataset. Models are trained using different tabular data modalities: whole-body radiomics, non-image data, and a combination of whole-body radiomics and non-image data. The best-performing model based on accuracy is highlighted in bold and reported in Figure 2.

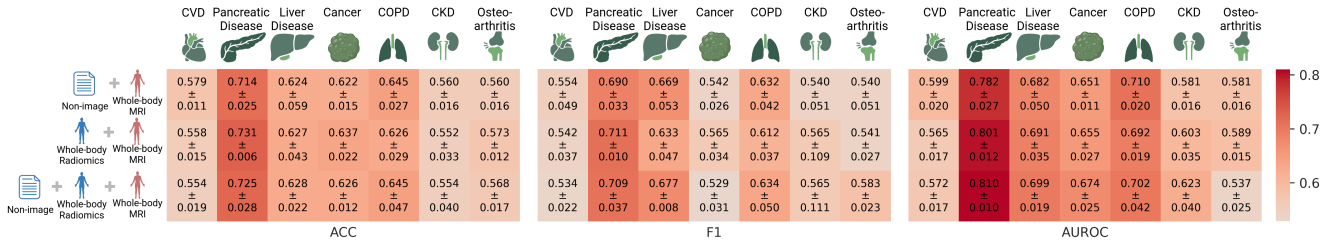

Supplementary Figure 3. Results of the best-performing fusion strategy combining whole-body MRI with non-image and whole-body radiomics for 3-year preclinical risk assessment for cardiovascular disease (CVD), pancreatic disease, liver disease, cancer, chronic obstructive pulmonary disease (COPD), chronic kidney disease (CKD), osteoarthritis.

Modality	Fusion Type	Metric		
		ACC	F1	AUROC
Non-image + Whole-body MRI	Joint	0.532 ± 0.009	0.546 ± 0.054	0.549 ± 0.014
Non-image + Whole-body MRI	**Late**	**0.579 ± 0.011**	0.554 ± 0.049	0.599 ± 0.020
Whole-body Radiomics + Whole-body MRI	Joint	0.536 ± 0.011	0.578 ± 0.033	0.562 ± 0.014
Whole-body Radiomics + Whole-body MRI	**Late**	**0.558 ± 0.015**	0.542 ± 0.037	0.565 ± 0.017
Non-image + Whole-body Radiomics + Whole-body MRI	Joint	0.518 ± 0.024	0.570 ± 0.067	0.536 ± 0.016
Non-image + Whole-body Radiomics + Whole-body MRI	**Late**	**0.554 ± 0.019**	0.534 ± 0.022	0.572 ± 0.017

Supplementary Table 8. Late and joint fusion strategies for cardiovascular disease (CVD). The best-performing model based on accuracy is highlighted in bold and reported in Figure 2. Late fusion uses the best-performing model for tabular data, shown in Supplementary Table 1, and the corresponding pre-trained image model for image data.

Modality	Fusion Type	Metric		
		ACC	F1	AUROC
Non-image + Whole-body MRI	**Joint**	**0.714 ± 0.025**	0.690 ± 0.033	0.782 ± 0.027
Non-image + Whole-body MRI	Late	0.708 ± 0.027	0.678 ± 0.036	0.780 ± 0.014
Whole-body Radiomics + Whole-body MRI	Joint	0.716 ± 0.007	0.699 ± 0.014	0.775 ± 0.017
Whole-body Radiomics + Whole-body MRI	**Late**	**0.731 ± 0.006**	0.711 ± 0.010	0.801 ± 0.012
Non-image + Whole-body Radiomics + Whole-body MRI	Joint	0.705 ± 0.022	0.682 ± 0.026	0.762 ± 0.025
Non-image + Whole-body Radiomics + Whole-body MRI	**Late**	**0.725 ± 0.028**	0.709 ± 0.037	0.810 ± 0.010

Supplementary Table 9. Late and joint fusion strategies for pancreatic disease. The best-performing model based on accuracy is highlighted in bold and reported in Figure 2. Late fusion uses the best-performing model for tabular data, shown in Supplementary Table 2, and the corresponding pre-trained image model for image data.

Modality	Fusion Type	Metric		
		ACC	F1	AUROC
Non-image + Whole-body MRI	**Joint**	**0.624 ± 0.059**	0.669 ± 0.053	0.682 ± 0.050
Non-image + Whole-body MRI	Late	0.624 ± 0.044	0.631 ± 0.046	0.699 ± 0.037
Whole-body Radiomics + Whole-body MRI	Joint	0.612 ± 0.043	0.619 ± 0.031	0.692 ± 0.033
Whole-body Radiomics + Whole-body MRI	**Late**	**0.627 ± 0.043**	0.633 ± 0.047	0.691 ± 0.035
Non-image + Whole-body Radiomics + Whole-body MRI	**Joint**	**0.628 ± 0.022**	0.677 ± 0.008	0.699 ± 0.019
Non-image + Whole-body Radiomics + Whole-body MRI	Late	0.627 ± 0.042	0.633 ± 0.047	0.698 ± 0.029

Supplementary Table 10. Late and joint fusion strategies for liver disease. The best-performing model based on accuracy is highlighted in bold and reported in Figure 2. Late fusion uses the best-performing model for tabular data, shown in Supplementary Table 3, and the corresponding pre-trained image model for image data.

Modality	Fusion Type	Metric		
		ACC	F1	AUROC
Non-image + Whole-body MRI	**Joint**	**0.622 ± 0.015**	0.542 ± 0.026	0.651 ± 0.011
Non-image + Whole-body MRI	Late	0.618 ± 0.019	0.583 ± 0.019	0.638 ± 0.008
Whole-body Radiomics + Whole-body MRI	**Joint**	**0.637 ± 0.022**	0.565 ± 0.034	0.655 ± 0.027
Whole-body Radiomics + Whole-body MRI	Late	0.627 ± 0.010	0.594 ± 0.014	0.665 ± 0.009
Non-image + Whole-body Radiomics + Whole-body MRI	**Joint**	**0.626 ± 0.012**	0.529 ± 0.031	0.674 ± 0.025
Non-image + Whole-body Radiomics + Whole-body MRI	Late	0.624 ± 0.007	0.585 ± 0.011	0.671 ± 0.013

Supplementary Table 11. Late and joint fusion strategies for cancer. The best-performing model based on accuracy is highlighted in bold and reported in Figure 2. Late fusion uses the best-performing model for tabular data, shown in Supplementary Table 4, and the corresponding pre-trained image model for image data.

Modality	Fusion Type	Metric		
		ACC	F1	AUROC
Non-image + Whole-body MRI	Joint	0.592 ± 0.044	0.591 ± 0.047	0.625 ± 0.022
Non-image + Whole-body MRI	**Late**	**0.645 ± 0.027**	0.632 ± 0.042	0.710 ± 0.020
Whole-body Radiomics + Whole-body MRI	Joint	0.574 ± 0.015	0.545 ± 0.048	0.614 ± 0.025
Whole-body Radiomics + Whole-body MRI	**Late**	**0.641 ± 0.031**	0.628 ± 0.032	0.701 ± 0.023
Non-image + Whole-body Radiomics + Whole-body MRI	Joint	0.591 ± 0.043	0.576 ± 0.028	0.614 ± 0.025
Non-image + Whole-body Radiomics + Whole-body MRI	**Late**	**0.645 ± 0.047**	0.634 ± 0.050	0.702 ± 0.042

Supplementary Table 12. Late and joint fusion strategies for chronic obstructive pulmonary disease (COPD). The best-performing model based on accuracy is highlighted in bold and reported in Figure 2. Late fusion uses the best-performing model for tabular data, shown in Supplementary Table 5, and the corresponding pre-trained image model for image data.

Modality	Fusion Type	Metric		
		ACC	F1	AUROC
Non-image + Whole-body MRI	**Joint**	**0.569 ± 0.010**	0.610 ± 0.026	0.584 ± 0.032
Non-image + Whole-body MRI	Late	0.544 ± 0.040	0.563 ± 0.110	0.598 ± 0.036
Whole-body Radiomics + Whole-body MRI	**Joint**	**0.577 ± 0.026**	0.586 ± 0.040	0.594 ± 0.025
Whole-body Radiomics + Whole-body MRI	Late	0.552 ± 0.033	0.565 ± 0.109	0.603 ± 0.035
Non-image + Whole-body Radiomics + Whole-body MRI	**Joint**	**0.559 ± 0.014**	0.603 ± 0.028	0.587 ± 0.030
Non-image + Whole-body Radiomics + Whole-body MRI	Late	0.554 ± 0.040	0.565 ± 0.111	0.623 ± 0.040

Supplementary Table 13. Late and joint fusion strategies for chronic kidney disease (CKD). The best-performing model based on accuracy is highlighted in bold and reported in Figure 2. Late fusion uses the best-performing model for tabular data, shown in Supplementary Table 6, and the corresponding pre-trained image model for image data.

Modality	Fusion Type	Metric		
		ACC	F1	AUROC
Non-image + Whole-body MRI	Joint	0.522 ± 0.004	0.463 ± 0.081	0.546 ± 0.005
Non-image + Whole-body MRI	**Late**	**0.560 ± 0.016**	0.540 ± 0.051	0.581 ± 0.016
Whole-body Radiomics + Whole-body MRI	Joint	0.514 ± 0.012	0.552 ± 0.083	0.536 ± 0.014
Whole-body Radiomics + Whole-body MRI	**Late**	**0.573 ± 0.012**	0.541 ± 0.027	0.589 ± 0.015
Non-image + Whole-body Radiomics + Whole-body MRI	Joint	0.511 ± 0.012	0.531 ± 0.086	0.529 ± 0.019
Non-image + Whole-body Radiomics + Whole-body MRI	**Late**	**0.568 ± 0.017**	0.583 ± 0.023	0.537 ± 0.025

Supplementary Table 14. Late and joint fusion strategies for chronic osteoarthritis. The best-performing model based on accuracy is highlighted in bold and reported in Figure 2. Late fusion uses the best-performing model for tabular data, shown in Supplementary Table 7, and the corresponding pre-trained image model for image data.

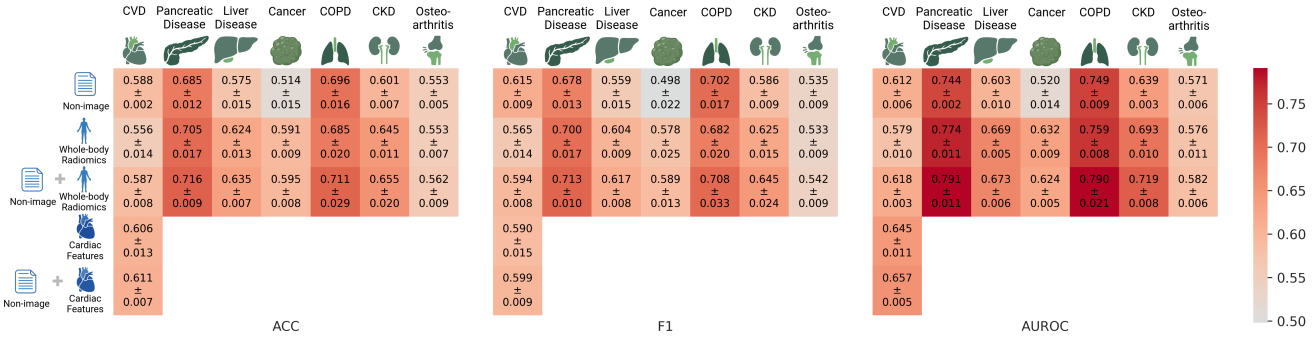

Supplementary Figure 4. Results of nested cross-validation of non-image and image-derived tabular models for 3-year preclinical risk assessment for cardiovascular disease (CVD), pancreatic disease, liver disease, cancer, chronic obstructive pulmonary disease (COPD), chronic kidney disease (CKD), osteoarthritis. Image-derived tabular features are represented by whole-body radiomics extracted from whole-body MRI, and cardiac features.

Supplementary Note 1

Supplementary Figures 5 and 6 present the category feature importances for "non-image + whole-body radiomics" and "whole-body radiomics" experiments, respectively. We apply the model-independent permutation-based feature importance method[2] to the best-performing model by evaluating the decrease in model accuracy when the category features' values are randomly shuffled.

The high importance rank of the non-image category, encompassing all non-image features, aligns with the predictive performance of the non-image data experiment compared to individually evaluated whole-body radiomics categories, shown in Figure 2. Furthermore, the notable importance of the non-image feature category across multiple diseases may be in part explained by its exceptionally rich data matrix, which covers a wide range of disease-related aspects.

The differences between the category feature importances of the "non-image + whole-body radiomics" and "whole-body radiomics" experiments highlight how non-imaging features may already capture information that overlaps with information that is extracted from imaging. For example, the fat category tends to rank lower in the "non-image + whole-body radiomics" experiment, assumably due to the presence of the variables, such as BMI or waist circumference, in the non-image data, as they already provide indirect yet informative proxies for fat distribution. Consequently, the added value of corresponding radiomic features may be reduced when both data sources are combined.

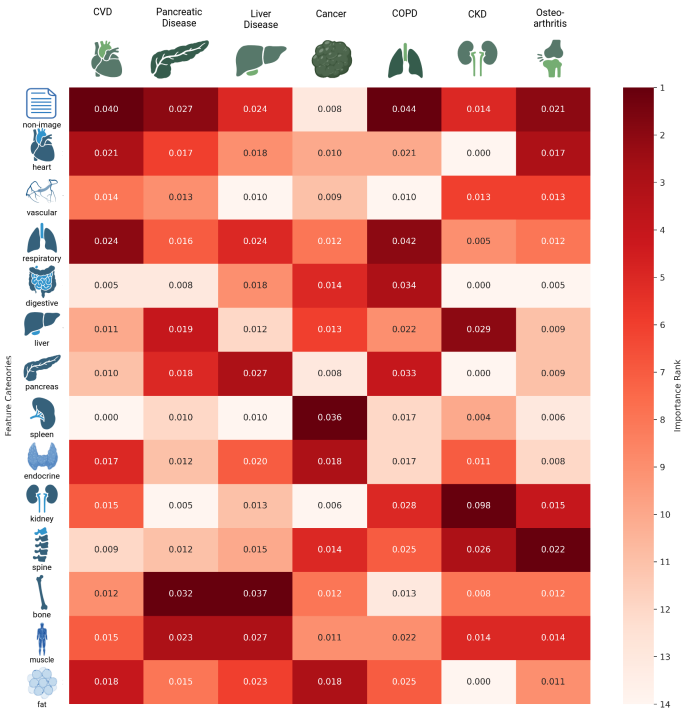

Supplementary Figure 5. Mean category-wise feature importances of the best-performing models by the category in the "non-image + whole-body radiomics" experiment. The color represents the rank based on the descending absolute values of the category feature importance. Rank 1 indicates the most important category.

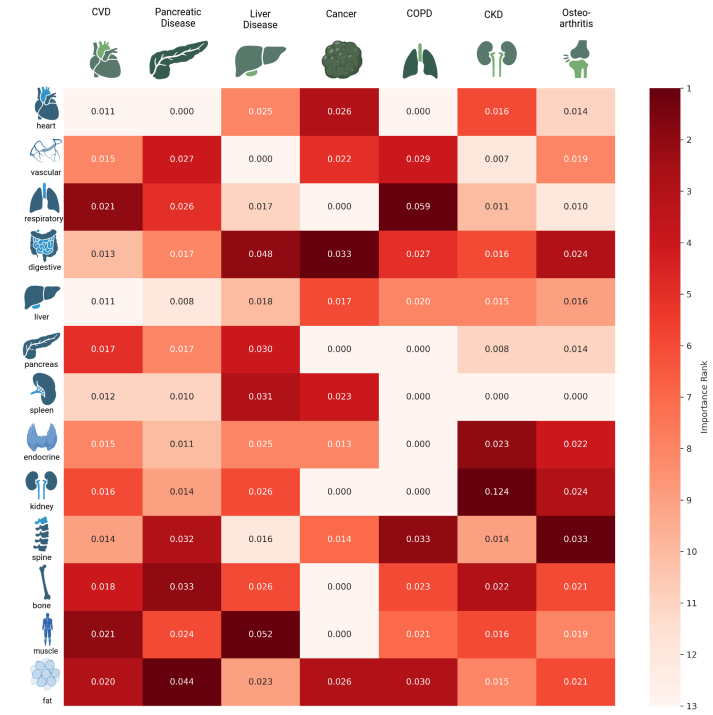

Supplementary Figure 6. Mean category-wise feature importances of the best-performing models by the category in the "whole-body radiomics" experiment. The color represents the rank based on the descending absolute values of the category feature importance. Rank 1 indicates the most important category.

Model	Hyperparameter Space
MLP	hidden_layer_sizes: {[64], [32], [64, 32], [64, 64], [128, 128], [128, 64, 32], {[256, 128, 64], [512, 128], [256, 256], [128, 512]} learning_rate_init: {1e-6, 1e-2} alpha: {0.1, 2.0} batch_size: {64, 256} activation: {relu} early_stopping: {true} validation_fraction: {0.1} n_iter_no_change: {10} solver: {adam} max_iter: {10000}
RF	n_estimators: {50, 300} max_depth: {3, 15} min_samples_split: {5, 30} min_samples_leaf: {5, 20} criterion: {gini, entropy, log_loss} max_features: {sqrt, log2} class_weight: {balanced} bootstrap: {true} oob_score: {true}
XGB	max_depth: {3, 15} min_child_weight: {3, 10} gamma: {1e-2, 5.0} subsample: {0.6, 0.95} colsample_bytree: {0.6, 0.95} learning_rate: {1e-4, 1e-1} n_estimators: {50, 300} reg_alpha: {1e-2, 5.0} reg_lambda: {1e-2, 5.0} objective: {binary:logistic} eval_metric: {logloss} tree_method: {exact} booster: {gbtree, dart}

Supplementary Table 15. Hyperparameter tuning space for experiments with non-image data and image-derived whole-body radiomics and cardiac features. The investigated models are Multi-layer Perceptron (MLP), Random Forest, eXtreme Gradient Boosting (XGB).

Modality	Data Augmentation	Optimizer	Scheduler	LR	WD	# Epochs	Dropout
Image	Random flips, blur, noise	AdamW	Cosine	0.001	0.0001	100	0.0
Image + Non-image	Random flips, blur, noise	AdamW	Cosine	0.0001	0.1	100	0.1

Supplementary Table 16. Hyperparameters of image (Whole-body MRI) and image + non-image models. LR: Learning Rate, WD: Weight Decay. The experimented model is ResNet 18 3D[3].

Supplementary Data 1

Supplementary Data 1 contains three tables. The full list of non-image and image-derived tabular features with the corresponding field IDs is provided in Table *Tabular Feature Description*. The full list of the ICD-10 and self-reported codes, alongside fields used to identify the preclinical disease risk assessment datasets, is provided in Table *Diagnostic codes related to disease categories*. The list of segmented organs and the feature categories is provided in Table *Whole-body Radiomics Features and Categories*.

Supplementary Data Availability

Supplementary Figure 1 is created in BioRender. Seletkov, D. (2025) https://BioRender.com/c7lrjbl. Supplementary Figure 2 is Created in BioRender. Seletkov, D. (2025) https://BioRender.com/fxchltj. Supplementary Figure 4 is created in BioRender. Seletkov, D. (2025) https://BioRender.com/bmovjrz. Supplementary Figure 5 is created in BioRender. Seletkov, D. (2025) https://BioRender.com/200osdb. Supplementary Figure 6 is created in BioRender. Seletkov, D. (2025) https://BioRender.com/v3ma0c7

Supplementary References

[1] Kwan, A. *et al.* Cardiovascular and hepatic disease associations by magnetic resonance imaging: A retrospective cohort study. *Front. Cardiovasc. Medicine* **9**, DOI: 10.3389/fcvm.2022.1009474 (2022).

[2] Breiman, L. Random forests. *Mach. Learn.* **45**, 5–32, DOI: 10.1023/A:1010950718922 (2001).

[3] Tran, D. *et al.* A closer look at spatiotemporal convolutions for action recognition. In *2018 IEEE/CVF Conference on Computer Vision and Pattern Recognition*, 6450–6459, DOI: 10.1109/CVPR.2018.00675 (2018).